Journal of
Synchrotron
Radiation

ISSN 0909-0495

Received 22 July 2004
Accepted 9 May 2005

Spherically bent analyzers for resonant inelastic X-ray scattering with intrinsic resolution below 200 meV

Emilie Collart,[a] Abhay Shukla,[a]* Frédéric Gélébart,[a] Marc Morand,[a] Cécile Malgrange,[a] Nathalie Bardou,[b] Ali Madouri[b] and Jean-Luc Pelouard[b]

[a]Laboratoire de Minéralogie-Cristallographie de Paris, Université Paris 6, Université Paris 7, CNRS, IPGP, Case 115, 4 Place Jussieu, 75252 Paris CEDEX 05, France, and [b]Laboratoire de Photonique et de Nanostructures, CNRS, Route de Nozay, 91460 Marcoussis, France.
E-mail: abhay.shukla@lmcp.jussieu.fr

Resonant inelastic X-ray scattering with very high energy resolution is a promising technique for investigating the electronic structure of strongly correlated materials. The demands for this technique are analyzers which deliver an energy resolution of the order of 200 meV full width at half-maximum or below, at energies corresponding to the *K*-edges of transition metals (Cu, Ni, Co *etc.*). To date, high resolution under these conditions has been achieved only with diced Ge analyzers working at the Cu *K*-edge. Here, by perfecting each aspect of the fabrication, it is shown that spherically bent Si analyzers can provide the required energy resolution. Such analyzers have been successfully produced and have greatly improved the energy resolution in standard spherically bent analyzers.

© 2005 International Union of Crystallography
Printed in Great Britain – all rights reserved

Keywords: RIXS; high-resolution analyzer; anodic bonding.

1. Background

A resonant inelastic X-ray scattering spectrometer uses a monochromatic beam at a fixed (resonant) energy incident on the sample. The radiation scattered by the sample is analyzed by a single crystal using a Bragg reflection and a detector. The analyzer is thus required to scan the scattered energy by changing the Bragg angle. Since the inelastic cross section is small, a spherical analyzer is used to increase the intercepted solid angle and to conserve experimental resolution by using Rowland circle geometry: source, analyzer and detector are mounted on a circle of diameter ρ, the radius of the analyzer being ρ in the case of the Johann geometry (Johann, 1931) illustrated in Fig. 1, which is often a sufficiently close approximation to the ideal figure (Johansson geometry). The analyzer is a key element of the spectrometer and has a determining role in the total energy resolution of the experiment. It has to fulfil both specular reflection conditions (at all points, incidence and reflection angles must be the same with reference to the reflection planes) and Bragg reflection conditions (deflection angle of the beam must be the same at all points of the surface). These conditions are only fulfilled for the single analyzer point on the Rowland circle in the case of the Johann geometry, and this leads to aberrations.

The five principal contributions to the total resolution are given in the following:

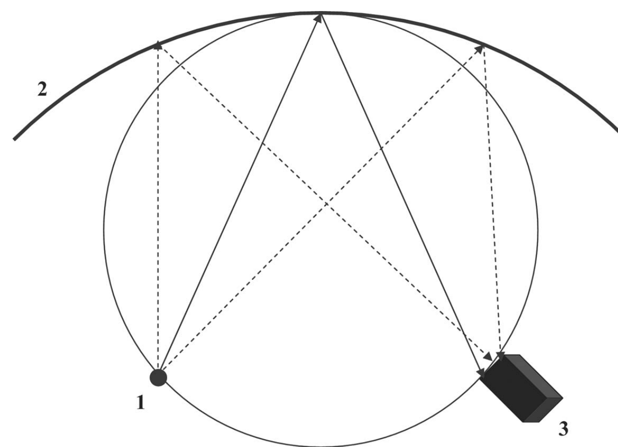

Figure 1
Rowland circle geometry. The incident beam is scattered by the sample (1), then analyzed by the spherically bent analyzer (2) with a radius which is twice that of the Rowland circle and detected by the detector (3). In the Johann geometry only one point of the analyzer is on the Rowland circle, giving rise to astigmatism and a contribution to the total resolution.

(i) Intrinsic resolution: contribution from the Darwin width and the effects of bending. The Darwin width is the intrinsic width of the rocking curve of the Bragg reflection for the perfect crystal. For the symmetric case (the only case considered in this work), it is given by

$$\omega_s = \frac{2C\lambda^2 r_e |F_{hkl}| \exp(-M)}{\pi V_0 \sin 2\theta_B},$$

where λ is the incident-beam wavelength, r_e is the electron classical radius, C is a polarization factor (1 for σ polarization and $\cos 2\theta_B$ for π polarization), $|F_{hkl}|$ is the structure factor modulus, $\exp(-M)$ is the Debye–Waller factor, V_0 is the cell volume and θ_B is the Bragg angle. Strained crystals, depending on the geometry and the conditions used, show a broadening of the reflectivity curve with respect to that of the perfect crystal. This can be calculated using the dynamical theory of diffraction [Takagi–Taupin (TT) equations], the approach that has been used in this paper. In the case of curved crystals, the strain gradient is only depth dependent and numerical calculations can be made using the one-dimensional version of the TT equations (Taupin, 1964). The program used here is described by Gronkowski (1991).

(ii) Contribution from the Johann error owing to the fact that only the center of the analyzer surface is on the Rowland circle. The intensity distribution e_J is (Suortti *et al.*, 1986)

$$e_J = |\varepsilon|^{-1/2}, \quad (1)$$

where ε is the angular Johann aberration in the horizontal direction: $\varepsilon \simeq -(1/2)(x/\rho)^2 \cot\theta_B$ with $0 \le x \le r$, r being the radius of the crystal analyzer and ρ its radius of curvature.

(iii) Axial Johann aberration in the direction perpendicular to the horizontal scattering plane. Here the angular aberration for spherical bending is also given by: $\varepsilon \simeq (1/2)(y/\rho)^2 \cot\theta_B$.

(iv) Contribution from the source which has a finite size. The footprint of the beam on the sample leads to a finite scattering volume related to the size of the footprint. The energy resolution is given *via* the differential Bragg law,

$$\Delta E = E \cot\theta_B \Delta\theta, \quad (2)$$

with E being the incident energy, θ_B the Bragg angle for the studied reflection and $\Delta\theta$ the angular width of the source as seen by a point on the analyzer.

(v) Energy spread of the incident beam provided by the monochromator.

With these contributions being independent, the total energy resolution is the convolution of these five functions. At this point we may estimate the resolution which could theoretically be reached with a spherically bent analyzer. We find that calculations predict full width at half-maximum (FWHM) ranging from about 50 meV to 60 meV according to the energy (Cu, Ni and Co K-edge) and corresponding reflections used. It is to be noted that, through the differential Bragg law, contributions (ii) to (iv) to energy resolution depend on the Bragg angle. Thus the larger the Bragg angle the smaller the contribution to the total resolution.

It is well known (see, for example, Masciovecchio *et al.*, 1996) that resolutions of the order of meV can be achieved for inelastic X-ray scattering under certain conditions. This is usually done by using small perfect crystals glued onto a spherical surface (diced analyzer) which is then a polygonal approximation to the perfect sphere of the Rowland circle geometry. This effectively eliminates the strain which broadens the intrinsic resolution. Other contributions to the total resolution are eliminated by working at very high Bragg angles (*e.g.* 89.95°). Finally, high-order reflection indices (888, 999 or 11,11,11) are used so as to obtain a very small Darwin width.

Unfortunately these ways of improving the energy resolution are not applicable to RIXS experiments because of the incident energy, which is fixed by the K-edge studied, and limits the possible Bragg angles to less than 80° [with the notable exception of the Cu K-edge, see for example Abbamonte *et al.* (1999) and Kim *et al.* (2002)]. Bragg's law gives a choice between several couples of Bragg angles and crystal reflections. It is obviously best to choose the reflection which provides a Bragg angle closest to backscattering for a given K-edge energy. However, in most cases this Bragg angle is not sufficiently close to backscattering to allow working with diced analyzers. The contribution to the total resolution owing to the size of the flat crystal cubes is too high. For example, at the Cu K-edge (8979 eV) and with a Rowland circle diameter of 2 m, taking 0.5 mm × 0.5mm as a typical size of the cubes on diced analyzers, the cube size contribution to the energy resolution is 124 meV for a Ge analyzer (θ_B = 86.832° on 733 reflection) and 495 meV for a Si analyzer (θ_B = 77.561° on 553 reflection). The cube size contribution is clearly of the same order or greater than the total energy resolution sought. At the Ni K-edge (8333 eV) we have contributions of 382 meV for Ge 642 and 441 meV for Si 551. Diced analyzers are thus not suitable in general for application to RIXS and we turn to spherically bent analyzers in our experiments.

RIXS measurements are routinely performed at a resolution of about 1 eV with bent Si crystals (Kao *et al.*, 1996; Hill *et al.*, 1996, 1998; Isaacs *et al.*, 1996; Enkisch *et al.*, 1999; Hämäläinen *et al.*, 2000; Döring *et al.*, 2004). As mentioned before, a much better resolution should potentially be available with such analyzers. We attribute this unsatisfactory value to the fabrication process of these analyzers which consists of gluing a silicon wafer onto a Pyrex substrate while bending.

Notwithstanding this, there have been reports of resolutions down to 300 meV FWHM in some RIXS experiments (Hämäläinen *et al.*, 1991; Bergman & Cramer, 1998; Caliebe *et al.*, 1998; Galambosi *et al.*, 2003; Diamant *et al.*, 2003). Several factors have to be noted before comparisons can be made. At low energy (Mn K-edge, 6539 eV for example) it is easier to obtain better resolution owing to reduced penetration of X-rays in the analyzer. Also, resolution can be bettered, as is often the case, by using masks on the analyzer or narrow slits in front of the detector to eliminate contributions from the bad part of the analyzer or to reduce the effects of cube size. These methods pay the price of reduced flux and do not address the central question of how to make a better analyzer. In the data shown in the following, the entire surface of the analyzer is used and the detector slits do not induce any reduction of flux. The energies measured vary from 7709 eV (Co K-edge) to 8979 eV (Cu K-edge). The results thus indicate the true overall quality of our analyzers.

The mediocre resolution of a standard Si analyzer arises for the two following reasons. Firstly, the layer of glue between

Table 1
K-edge energy and optimal Bragg angles θ_B for Co, Ni and Cu.

A comparison is made between Si and Ge crystals for the three transition metals.

Material	Co	Ni	Cu
E K-edge (eV)	7709	8333	8979
Si θ (°)	76.169	78.040	77.561
hkl	533	551	553
Darwin width for Si (meV)	31	25	20
Ge θ (°)	79.85	79.609	86.832
hkl	444	642	733
Darwin width for Ge (meV)	81	66	35

the silicon and Pyrex induces strains and bulges on the surface of the analyzer and, secondly, bad wafer polishing causes slope errors. We can act on both to improve energy resolution, however. We eliminate the glue layer by using the anodic bonding technique widely used in the semiconductor industry for bonding metallic-type wafers to insulating substrates containing alkali metal ions. This process has previously been used by M. Kocsis and R. Verbeni at the ESRF, Grenoble, to produce spherically bent analyzers. We also use a large bending radius of 2 m in order to reduce strains and resulting distortions arising from curvature of the wafer surfaces. This also has the advantage of reducing the contribution owing to angular source size: it is halved at 2 m with respect to 1 m. Finally a well known empirical rule for bending Si wafers tells us that the elastic limit is reached for a wafer thickness which is above 10^{-3} times the bending radius. To be well within this limit, we chose wafers of a thickness of 500 µm.

2. Experimental details

Before constructing an analyzer, a crucial factor is the choice between silicon and germanium. As mentioned before, one of the most important parameters is the Bragg angle for reflection in the chosen material: it is important to have Bragg angles as close as possible to backscattering. Table 1 shows a comparison between Ge and Si reflection indices and Bragg angles at the *K*-edges for Cu, Ni and Co. For Cu there is a significant difference between Ge and Si but for Ni and Co the advantage of using Ge is limited. Moreover, silicon, owing to its large-scale use, has higher crystal purity, can be polished to a greater degree of perfection and is much cheaper. We therefore chose silicon as the material for our analyzers. Futhermore, the bonding technique used here is indicated for silicon.

Anodic bonding has been a much employed technique in the silicon industry (Wallis & Pomerantz, 1969) and is still widely used for bonding glass to conductive material owing to the good bond quality (silicon-on-insulator bonding or SOI bonding). It allows the joining of two solids without intervening layers like glue and is typically performed between a sodium-bearing glass substrate (here, Pyrex 7740 from Corning) and a silicon wafer, the two materials having a fairly good match of thermal expansion. At high temperatures, Na_2O in Pyrex glass decomposes into one O^{2-} and two Na^+ ions. Mobility of the smaller sodium ions is high and the presence of an electric field across the glass substrate (Albaugh *et al.*, 1988) makes them migrate towards the cathode at its back. They leave behind a negative space charge in the region of the interface between Si and glass arising from the static oxygen ions which create a high electrostatic field with the positive charges in the silicon wafer. This field pulls the wafer into more and more intimate contact with the substrate, ultimately leading to the formation of stable Si—O—Si bonds.

In our experiment, silicon wafers were polished on both sides. Their diameter was 100 mm and they were 500 µm thick with a total thickness variation of less than 3 µm. They were cut perpendicular to the [553], [551] and [533] directions for Cu *K*-edge, Ni *K*-edge and Co *K*-edge measurements, respectively. The Pyrex glass matrix had the same diameter as the silicon wafers. The press used to perform the bonding is schematically represented in Fig. 2. The silicon wafer is pressed between two Pyrex pieces, one concave and the other convex, with the same radius of curvature (2 m here). Pressure is applied from the top, heating from the bottom and the potential difference is generated between a cathode connected to the back of the substrate and the Si wafer which is earthed.

First, the surfaces to be bonded have to undergo the standard chemical preparation (Gracias *et al.*, 2000) commonly used for cleaning silicon. Then the silicon wafer and the concave Pyrex substrate are soaked in a standard ammonium peroxide bath (Anthony, 1983; Wei *et al.*, 2003) which oxidizes the surfaces and traps any remaining impurities. Next, this oxide layer is removed in a hydrofluoric acid bath.

The silicon wafer is then placed between the concave substrate to which it is to be bonded and the convex form. The wafer, insulated from the convex form, is earthed while the cathode is connected to a negative potential (around −1.5 kV). We carry out bonding in a clean room of class 1000

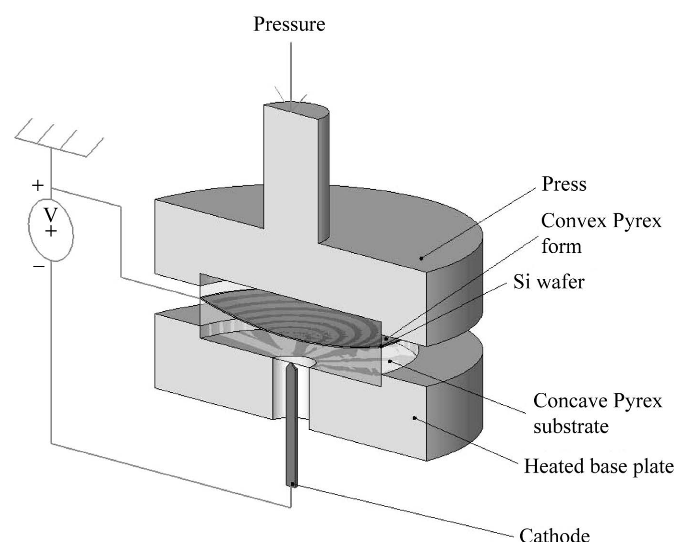

Figure 2
A press for anodic bonding. The silicon wafer is placed inside the press between the concave and convex forms. The base plate is heated.

since dust particles trapped between the surfaces lead to deformations and an unusable analyzer. The whole sandwich is then placed in the press, the pressure applied to the silicon wafer and the heating turned on. After thermalization at ~573–623 K at the Pyrex–silicon interface, the potential difference is applied leading immediately to a current owing to the mobile Na^+ ions. Bonding is over when the current intensity is no longer significant. During the bonding phase we carefully monitored the current as it denotes both quality and strength of the bonding process. The relevant feature for this measurement is the total transferred charge: the greater it is, the tighter the bonding.

3. Measurements

For a real RIXS experiment we are interested in the total resolution that can be obtained. We also need to maximize flux at the same time and the optimal experimental conditions are those where the spread of incident energy and the intrinsic resolution of the analyzer are of the same order of magnitude and all geometric contributions are minimized as far as possible. The total energy resolution is then higher than the intrinsic analyzer resolution. The measurements shown hereafter take into account these considerations. To extract the intrinsic resolution of the analyzer a deconvolution procedure would be needed. Since the broadening is of the order of the intrinsic resolution the deconvolution procedure does not give a unique solution. We estimate this intrinsic resolution by assuming the line shape to be Gaussian. We convolute a Gaussian function of varying FWHM with the other significant contributions to the resolution, namely the incident bandwidth (measured) and the source size (Gaussian), until a good match with the total experimental resolution is obtained. The FWHM thus extracted is used to quantify the intrinsic resolution of the analyzer. If we use a Lorentzian line shape, the estimated FWHM is smaller by about 30%, so the Gaussian line shape should give a reliable superior bound.

In the following results the Johann error was found to be negligible compared with the other contributions to the energy resolution and was not taken into account.

Measurements on analyzer Si 553 (Cu *K*-edge) were performed at SPring-8 (Japan) at beamline BL12XU. The analyzing plane was horizontal and the incident energy was tuned to 8979 eV, giving a Bragg angle of 77.56°. The beamline was equipped with a Si 111 pre-monochromator followed by a Si 400 double-crystal channel-cut monochromator. The incident bandwidth was measured by analyzing the incident beam with a perfect crystal Si 555 reflection in almost exact backscattering at 9885.3 eV, giving an energy spread of 167 meV FWHM (dashed line, Fig. 3). The beam was 120 μm wide, thus the source size contribution to the total resolution was 121 meV FWHM at the working energy (dashed-dotted line, Fig. 3). The theoretical intrinsic energy resolution was calculated to have a FWHM of 59 meV (dotted curve, Fig. 3). The solid curve in Fig. 3 represents the convolution of these three contributions and predicts under our experimental conditions a total energy resolution of 232 meV FWHM at the Cu *K*-edge. The last curve in Fig. 3 is the experimental resolution (solid line with circles), and displays an overall FWHM of 291 meV. With the assumption of a Gaussian shape for the intrinsic resolution, we find a 218 meV FWHM for this analyzer, to be compared with the theoretical value of 59 meV.

Measurements on the Si 533 analyzer (Co *K*-edge) were performed at the ESRF (France) at beamline ID16. The analyzing plane was horizontal and the incident energy was tuned to 7709 eV, which gives a Bragg angle of 76.17°. The beamline was equipped with a Si 111 pre-monochromator followed by a single-crystal Si 440 channel-cut monochromator. The incident bandwidth was measured by analyzing the incident beam with a perfect crystal Si 444 reflection in almost exact backscattering at 7909 eV, giving an energy spread of 169 meV FWHM (dashed line, Fig. 4). The beam was 180 μm wide, thus the source size contribution to the total resolution was 171 meV at the working energy (dashed-dotted line, Fig. 4). Theoretical intrinsic energy resolution was calculated to have a FWHM of 50 meV (dotted curve, Fig. 4). Fig. 4 compares the convolution of the three latter contributions (solid line) with the experimental resolution (solid line with circles). Assuming a Gaussian shape for the intrinsic resolution of this analyzer, it is found to have a FWHM of 161 meV.

Measurements on the Si 551 analyzer (Ni *K*-edge) were performed at the APS (USA) in sector 18-ID. The analyzing plane was vertical and the incident energy was tuned to

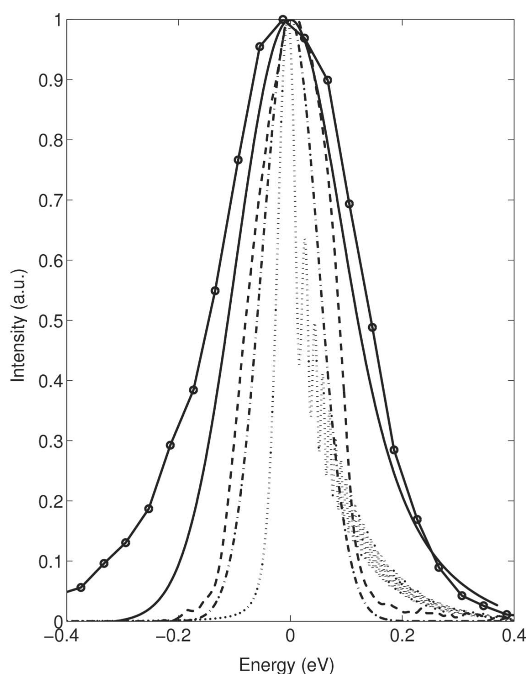

Figure 3
Si (553) analyzer for the Cu *K*-edge. Dashed line: energy spread of the incident beam (FWHM = 167 meV); dashed-dotted line: source size contribution (FWHM = 121 meV); dotted line: intrinsic resolution of the bent crystal calculated by the TT method (FWHM = 59 meV); solid line: total calculated resolution from convolution of all contributions (FWHM = 232 meV); solid line with circles: experimental resolution, FWHM = 291 meV. All curves have been normalized to maximum for better visibility.

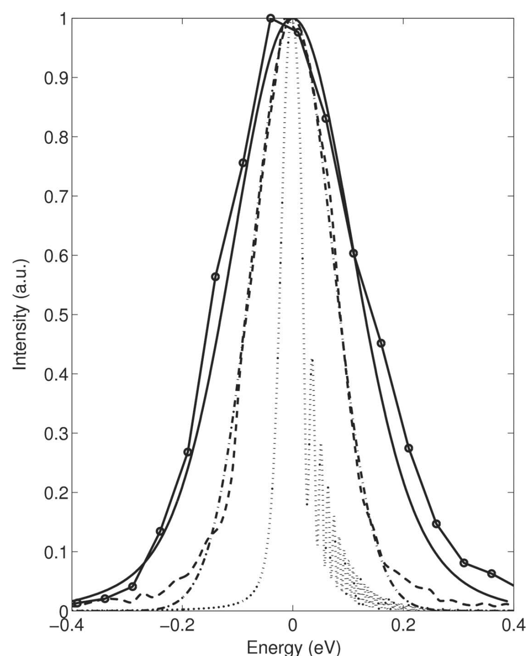

Figure 4
Si (533) analyzer for the Co *K*-edge. Dashed line: energy spread of the incident beam (FWHM = 169 meV); dashed-dotted line: source size contribution (FWHM = 171 meV); dotted line: intrinsic resolution of the bent crystal calculated by the TT method (FWHM = 50 meV); solid line: total calculated resolution from convolution of all contributions (FWHM = 259 meV); solid line with circles: experimental resolution, FWHM = 297 meV. All curves have been normalized to maximum for better visibility.

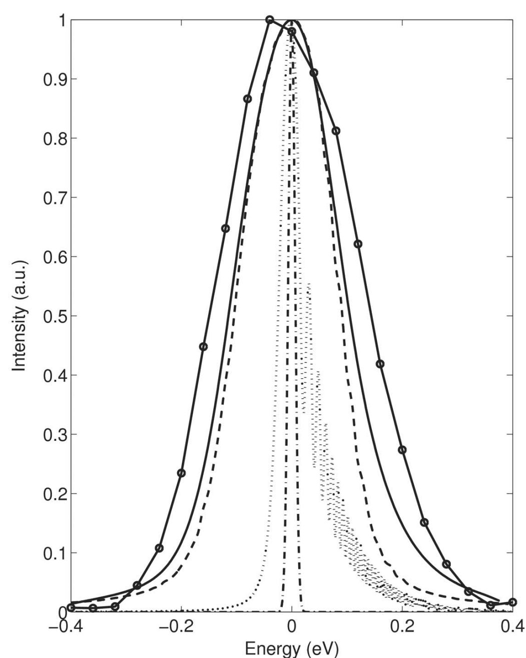

Figure 5
Si (551) analyzer for the Ni *K*-edge. Dashed line: energy spread of the incident beam (FWHM = 195 meV); dashed-dotted line: source size contribution (FWHM = 14 meV); dotted line: intrinsic resolution of the bent crystal calculated by the TT method (FWHM = 59 meV); solid line: total calculated resolution from convolution of all contributions (FWHM = 219 meV); solid line with circles: experimental resolution, FWHM = 291 meV. All curves have been normalized to maximum for better visibility.

8156 eV which gives a Bragg angle of 88.14°. The beamline was equipped with a double-crystal channel-cut Si 111 pre-monochromator followed by a single-crystal Si 400 channel-cut monochromator. The incident bandwidth was measured by analyzing the incident beam with a perfect crystal Si 444 reflection at 8156 eV, giving an energy spread of 195 meV (dashed line, Fig. 5). The beam was 100 µm in the vertical direction, thus the source size contribution to the total resolution was 14 meV FWHM at the working energy (dashed-dotted line, Fig. 5). In this case the theoretical intrinsic energy resolution was calculated to have a FWHM of 59 meV (dotted curve, Fig. 5). With similar assumptions as before, the intrinsic resolution of this analyzer was found to have a FWHM of 217 meV.

Although the calculated intrinsic resolution may be to some extent an underestimation owing to minor simplifications, wafer quality is still the limiting factor for analyzer performance. The bonding between our glass substrate and the Si wafers is perfect, as revealed by visual inspection of the bonded interface through the back of the substrate. Remaining imperfections come from wafer quality and eventually polishing errors in the substrates. Some traces of polishing were visible on several Si wafers and we have found measured intrinsic resolutions still substantially higher than calculated ones. This in turn leads us to believe that still better performance can be achieved with such analyzers.

4. Conclusion

We have made spherically bent Si single-crystal analyzers with a bending radius of 2 m for measuring resonant inelastic X-ray scattering at *K*-edges of transition metals. We have shown that it is possible to routinely obtain an intrinsic resolution of the order of 200 meV FWHM and below. This result has been obtained by perfecting each aspect of analyzer fabrication, including wafer preparation, and the bonding technique. These analyzers open new horizons for RIXS in transition metal compounds. Furthermore, by working on wafer perfection we hope to obtain intrinsic resolution of the order of 100 meV FWHM with these analyzers.

We acknowledge M. Idir and T. Moreno for calculations, and D. Chandesris and R. Verbeni for discussions. We also thank Y. Caï and H. Ishii for help at SPring-8, G. Vankó at the ESRF and A. Deb and S. Cramer for the run at the APS. This work benefited from a CNRS/JSPS No. 16030 research grant.

References

Abbamonte, P., Burns, C. A., Isaacs, E. D., Platzman, P. M., Miller, L. L., Cheong, S. W. & Klein, M. V. (1999). *Phys. Rev. Lett.* **83**, 860–863.

Albaugh, K. B., Cade, P. E. & Rasmussen, D. H. (1988). Solid State Sensor and Actuator Workshop, Hilton Head Island, SC, USA, pp. 109–110. IEEE Report.

Anthony, T. R. (1983). *J. Appl. Phys.* **54**, 2419–2428.

Bergman, U. & Cramer, S. P. (1998). *Proc. SPIE*, **3448**, 198–209.

Caliebe, W. A., Kao, C.-C., Hastings, J. B., Taguchi, M., Kotani, A., Uozumi, T. & de Groot, F. M. F. (1998). *Phys. Rev. B*, **58**, 13452–13458.

Diamant, R., Huotari, S., Hämäläinen, K., Sharon, R., Kao, C. C. & Deusch, M. (2003). *Phys. Rev. Lett.* **91**, 193001-1–193001-4.
Döring, G., Sternemann, C., Kaprolat, A., Mattila, A., Hämäläinen, K. & Schülke, W. (2004). *Phys. Rev. B*, **70**, 85115-1–85115-15.
Enkisch, H., Kaprolat, A., Schülke, W., Krisch, M. H. & Lorenzen, M. (1999). *Phys. Rev. B*, **60**, 8624–8627.
Galambosi, S., Sutinen, H., Mattila, A., Hämäläinen, K., Sharon, R., Kao, C. C. & Deusch, M. (2003). *Phys. Rev. A*, **67**, 22510-1–22510-5.
Gracias, A. C., Rios, A. N., Maia, I. A. & Senna, J. R. (2000). *Rev. Bras. Aplic. Vacuo*, **19**, 19–22.
Gronkowski, J. (1991). *Phys. Rep.* **206**, 1–41.
Hämäläinen, K., Siddons, D. P., Hastings, J. B. & Berman, L. E. (1991). *Phys. Rev. Lett.* **67**, 2850–2853.
Hämäläinen, K., Hill, J. P., Huotari, S., Kao, C.-C., Berman, L. E., Kotani, A., Idé, T., Peng, J. L. & Greene, R. L. (2000). *Phys. Rev. B*, **61**, 1836–1840.
Hill, J. P., Kao, C.-C., Caliebe, C., Gibbs, D. & Hastings, J. B. (1996). *Phys. Rev. Lett.* **77**, 3665–3668.
Hill, J. P., Kao, C.-C., Caliebe, W. A. L., Matsubara, M., Kotani, A., Peng, J. L. & Greene, R. L. (1998). *Phys. Rev. Lett.* **80**, 4967–4970.
Isaacs, E. D., Platzman, P. M., Metcalf, P. & Honing, J. M. (1996). *Phys. Rev. Lett.* **76**, 4211–4214.
Johann, H. H. (1931). *Z. Phys.* **69**, 185–206.
Kao, C.-C., Caliebe, W. A. L. & Hastings, J. B. (1996). *Phys. Rev. B*, **54**, 16361–16364.
Kim, Y. J., Hill, J. P., Burns, C. A., Wakimto, S., Birgeneau, R. J., Casa, D., Grog, T. & Venkataraman, C. T. (2002). *Phys. Rev. Lett.* **89**, 177003-1–177003-4.
Masciovecchio, C., Bergmann, U., Krisch, M., Ruocco, G., Sette, F. & Verbeni, R. (1996). *Nucl. Instrum. Methods*, B**111**, 181–186.
Suortti, P., Pattison, P. & Weyrich, W. (1986). *J. Appl. Cryst.* **19**, 343–352.
Taupin, D. (1964). *Bull. Soc. Fr. Mineral. Cristallogr.* **87**, 469–511.
Wallis, G. & Pomerantz, D. I. (1969). *J. Appl. Phys.* **40**, 3946–3949.
Wei, J., Nai, M. L., Wong, C. K. & Lee, L. C. (2003). *J. Micromech. Microeng.* **13**, 217–222.